Pellet Printing for Soft Robotic Devices

*Yijia Wu, Ju-Hung Chen, Ariana Olivares, Katherine Kostak, Stefan Pedicone, Savita V. Kendre, and Markus P. Nemitz**

Y. Wu, J. Chen, A. Olivares, K. Kostak, S. Pedicone, Dr. S. V. Kendre, Prof. M. P. Nemitz

Department of Mechanical Engineering, Tufts University, Medford, MA 02155, USA

Email Address: markus.nemitz@tufts.edu

Keywords: *fused granulate fabrication, additive manufacturing, 3D printing, thermoplastic elastomers, soft robots*

Rapid prototyping of soft devices is often constrained by manual fabrication or additive manufacturing methods that are limited in material choice or require extensive post-processing. Fused Granulate Fabrication offers a scalable alternative by extruding thermoplastic pellets through a screw-based extruder, enabling continuous, high-throughput printing and access to a broad range of commercially available materials, from rigid plastics to silicone-soft elastomers (Shore hardness down to 6A). Reliable 3D printing of airtight pneumatic soft structures at volumetric flow rates up to 5 mm^3/s is demonstrated by addressing inconsistent extrusion and stringing issues through a combination of hardware optimization and a materials-centered printing strategy. Extrusion and oozing tests are used to construct material-specific oozing performance profiles, establishing practical guidelines for material selection in FGF printing, and are linked to key rheological descriptors. The mechanical performance of thermoplastic styrenic block copolymer pellets is characterized, revealing Mullins-effect-induced softening, and fabricated pneumatic actuators exhibit durability exceeding 100,000 bending cycles. Demonstrations include a pneumatically actuated robotic hand, a multi-chamber robotic fish, and a soft pressure cuff. FGF enables the digital fabrication of large-scale, airtight soft devices using commercially available thermoplastic pellets, providing a versatile, cost-effective, and scalable alternative to soft lithography with mechanical performance comparable to silicone elastomers.

1 Introduction

Soft robotics is a transformative field that enables the creation of adaptable, compliant, and biomimetic systems [1], with applications spanning medical devices [2], assistive wearables [3], robotic locomotion [4], and manipulation [5], among others. The intrinsic deformability of soft materials enhances safety in human-robot interaction [6], improves resilience to mechanical impact [7], and allows robots to change their shape [8], thereby enabling functionalities beyond the reach of traditional robots with rigid body plans. Despite these advances, the fabrication of soft systems, particularly those requiring airtight properties and materials within the Shore 00 hardness range, remains a major challenge. Soft lithography has long been used to produce such systems, but it involves laborious fabrication steps and depends heavily on operator skill, limiting scalability, reproducibility, and broader adoption beyond specialized laboratories [9]. As a result, many state-of-the-art demonstrations, including multi-gait soft robots [8], bistable valves [10], and soft grippers [11], still rely on custom molds, extensive post-processing, and manual assembly.

Digital fabrication techniques including Fused Filament Fabrication (FFF), Direct Ink Writing (DIW), Stereolithography (SLA), Material Jetting (MJ), and Selective Laser Sintering (SLS), have been explored as mold-free alternatives to soft lithography for fabricating soft devices. However, each method presents fundamental trade-offs in material compatibility, geometric fidelity, and printing reliability that have limited their widespread use [12, 13, 14]. While FFF remains popular due to its low cost and accessibility [15, 16, 17, 18, 19, 20, 21, 22, 23], its performance is constrained by filament mechanics. Commercial soft filaments are typically thermoplastic polyurethanes (TPUs) with Shore hardness $\geq$ 60A, which are relatively stiff compared to silicones and often lead to extrusion issues such as buckling and jamming during printing [24]. DIW is a versatile technique compatible with a wide range of soft materials, such as silicones, hydrogels, and liquid-crystal elastomers, and particularly suitable for exploring new formulations. However, DIW generally requires careful rheological tuning to achieve printability, and commercial materials or materials formulated by non-experts often suffer from flow instabilities or demand long, process-sensitive curing steps [25, 26, 27, 28, 29, 30]. SLA and MJ offer high print resolution but rely on brittle photopolymers with viscoelastic material characteristics, poor fatigue resistance, and UV degradation [31, 32, 33]. SLS avoids support structures but is limited by challenges in powder removal and a narrow range of available soft elastomers ($\geq 40A$). Although these techniques have enabled important advances in soft device manufacturing, their material and process constraints and availability continue to limit the geometric complexity, mechanical performance, and reproducibility of fabricated devices.

These challenges become more severe in fluidically driven soft systems, where airtightness and geometric precision are essential for integrating channels and enclosed chambers within a single build. SLA, MJ, SLS, and DIW struggle with internal cavities where residual resin, powder, or ink becomes trapped, especially in long, narrow channels and complex internal networks [34, 35]. Although MJ supports the use of support materials, their removal still hinders the fabrication of fully enclosed chambers. FFF methods mitigate this issue but introduce their own challenges including leakage and limited print reliability for complex geometries. 3D printing airtight structures reliably requires slow print speeds (<20 mm/s) and restrictive design rules, such as multi-layered walls [18] or Euler-path toolpaths to minimize interfacial voids [22]. Other strategies to improve airtightness include gravity-assisted layer sealing [36] and vision-based closed-loop control for real-time defect correction [24]. Although FFF has become more reliable for fabricating soft devices, it remains fundamentally limited in material selection, as it can only print materials with high Shore hardness, far from the low hardness characteristic of silicones.

A promising alternative to established printing strategies is Fused Granulate Fabrication (FGF). FGF has been primarily used in industry rather than in research laboratories. It offers several industry relevant advantages including high throughput, low material cost, broad material availability, existing expertise from injection molding, and the capability to print at large scales. FGF processes raw pellets through an extrusion screw, achieving higher extrusion rates and access to a wider range of thermoplastics than FFF [37, 38]. Thermoplastic styrenic block copolymers (TPS) can achieve lower Shore hardness values than other classes of thermoplastic elastomers (TPEs) [39]. Previous studies have used desktop FGF printers to demonstrate their potential for printing specialized materials [40, 41], including conductive pellets for sensorized actuators [39, 42, 43] and ultra-soft membranes within the Shore 00–30 range [44]. However, these efforts have been isolated, with limited exploration of geometry and material diversity [43, 44, 41], leaving much of the thermoplastic elastomer landscape across the Shore 00 and A scales unexamined. Although many thermoplastic pellets exist with Shore hardness values comparable to silicones, their suitability for desktop printing remains largely unknown. Most thermoplastic pellets are formulated for injection molding rather than for additive manufacturing. The relationship between material rheology, mechanical properties, and print fidelity in FGF is not yet well studied, making it unclear which parameters most strongly affect print reliability. We need a systematic evaluation and benchmarking of key performance metrics including elasticity, strain softening, fatigue resistance, and processability, to establish the potential of thermoplastic pellets as next-generation materials for soft devices. In contrast to FFF printers and filaments, which have matured with well-defined process parameters, FGF

remains at an early stage of technological development.

Commercially available pellet extruders and compatible desktop 3D printers are limited. The few reported FGF systems rely on custom-built extruders, which reduces reproducibility and hinders standardization [41, 44]. The high extrusion rates typical of pellet extruders, while beneficial for throughput, increase the likelihood of print defects. Severe stringing has been observed in FGF-printed pneumatic actuators [41]. Hardware modifications to the 3D printer such as custom needle valves have been proposed to reduce oozing, but these solutions have not been broadly tested with different materials and are difficult to reproduce [45]. Only a few studies have demonstrated mechanically complex geometries. Large-scale, fluidically driven soft devices have remained mostly unexplored. As a result, the capability of FGF to reliably fabricate high-quality soft devices remains uncertain and has not yet achieved widespread adoption within the soft robotics community or beyond.

In this study, we address the challenges of FGF and demonstrate the feasibility of using a desktop printer to fabricate large, geometrically complex, fluidically driven soft devices. By systematically examining extrusion stability, stringing behavior, and material-dependent printability, the primary failure modes limiting airtight fabrication are identified and mitigated. Rather than relying solely on process tuning, this work adopts a materials-centered approach, showing that appropriate selection of commercially available thermoplastic styrenic block copolymer pellets, characterized by high low-shear viscosity and strong shear-thinning behavior, can effectively suppress stringing while maintaining high extrusion throughput. Using this strategy, pellets spanning Shore hardness values from 6A (00–55) to 50A (00–85) are printed at flow rates exceeding those typically achievable with FFF and DIW (Figure 1), enabling robust and repeatable fabrication.

To evaluate the suitability of TPS materials for fabricating soft devices, we characterized their mechanical properties through tensile testing. We 3D printed pneumatic actuators, measured their bending response, and compared the results with numerical simulations. Fatigue testing confirmed actuator durability beyond 100,000 actuation cycles. Tensile cycling and actuator bending experiments revealed a pronounced reduction in Young's modulus after the first stress cycle. This observation is attributed to the Mullins effect and emphasizes the need to activate the printed device once before it is used in operation. We demonstrated the versatility of FGF by 3D printing a pneumatically driven soft hand with 15 individually addressable segments, a multi-chamber robotic fish with an articulated fin, and a pressure cuff for measuring systolic pressure. This study shows that FGF provides a robust, accessible, and cost-effective method for rapidly prototyping large soft devices (tens of centimeters). With tens of thousands

of thermoplastic pellets commercially available, including materials with silicone-like softness, FGF unlocks a broad and previously inaccessible material palette for applications in robotics, medical devices, wearables, and beyond.

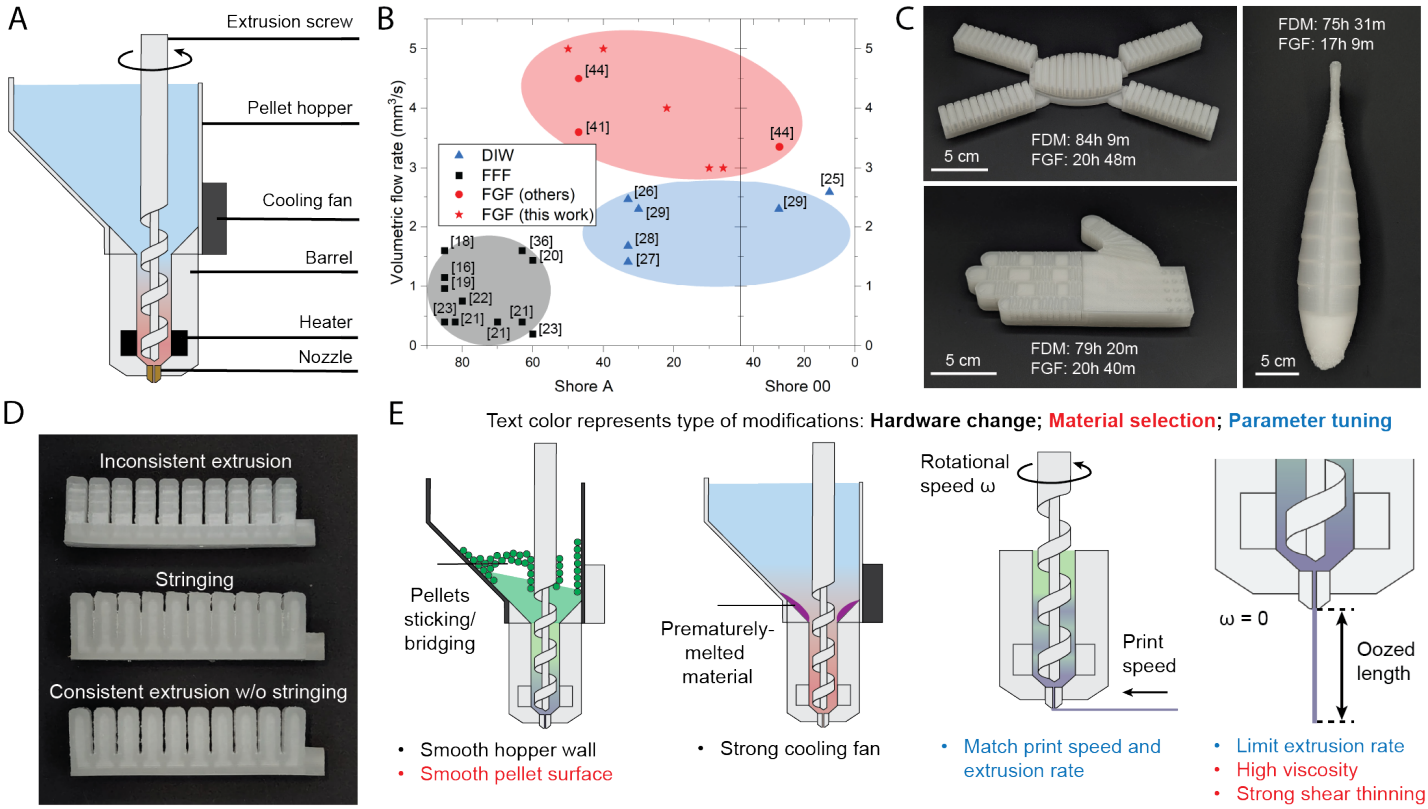

Figure 1: **Overview of the Fused Granulate Fabrication (FGF) printing process.** (A) Schematic of pellet extruder. (B) Estimated volumetric flow rate versus Shore A hardness from prior FFF and FGF studies on airtight soft robot fabrication, highlighting that FGF achieves higher volumetric flow rates while supporting softer materials than FFF. (C) Example of large-scale complex geometries printed with FGF, demonstrating that FGF significantly accelerates the fabrication of large soft structures. Print parameters are summarized in Supporting Information, Table S2. (D) Images of printed pneumatic actuators highlighting two common defects, inconsistent extrusion and stringing, that can compromise functionality, alongside an optimized print demonstrating successful mitigation through tuning. (E) Causes and solutions we implemented for inconsistent extrusion and stringing issues.

2 Pellet printing with soft materials

FGF, or pellet printing, operates on the same layer-by-layer deposition principle as FFF but uses thermoplastic pellets instead of filament feedstock. Pellets are fed by gravity or pneumatics into a screw-driven extruder, where they are melted and deposited through a heated nozzle (**Figure 1A**). This screw-based extrusion decouples material rigidity from processability, enabling the reliable printing of soft thermoplastic elastomers with stiffness comparable to silicones. In contrast, filament-fed FFF systems are prone to buckling when processing soft materials. To quantify this advantage, we analyzed published studies reporting airtight soft robotic components fabricated via DIW, FFF, or FGF. Volumetric flow

rates Q (mm^3/s) were estimated from reported nozzle diameters d (mm), layer heights h (mm), and print speeds v (mm/s) using their relation $Q = d \times h \times v$, assuming the extrusion width equals the nozzle diameter. The resulting comparison of volumetric flow rate versus material Shore hardness shows that FGF consistently achieves higher flow rates, even for softer materials (**Figure 1B**). FGF reduced the fabrication time of our demonstrators from several days using FFF to a single day (**Figure 1C**). While FGF offers several advantages over FFF including higher flow rates and broader compatibility with soft materials, it remains challenging to achieve consistent, high-quality prints. To promote the broader adoption of FGF for fabricating soft devices, we used a commercially available pellet extruder, a standard 3D printer, and commercially available soft thermoplastic pellets in our experiments. Although small, flat structures can be fabricated reliably, longer print durations and increased structural complexity lead to recurring issues such as mid-print failures, leakage, and stringing. We identified two main causes of these defects: inconsistent extrusion and stringing (**Figure 1D**). Severe occurrences of either can result in complete print failure, while milder cases compromise airtightness and device performance. Overcoming these challenges requires a coordinated strategy combining hardware modifications, material selection, and process parameter optimization (**Figure 1E**).

2.1 Enabling consistent extrusion

Inconsistent extrusion leads to non-uniform wall thickness, which can cause leakage in under-extruded regions or require higher actuation pressures in over-extruded areas of the printed soft device. We mitigated this issue through a three-step approach addressing feeding, melting, and extrusion: (1) improving pellet feeding by redesigning the print head hopper with smoother walls and selecting pellets with low surface friction; (2) preventing premature melting by enhancing active cooling using a higher performing fan; and (3) calibrating extrusion flow to match print speed, ensuring consistent material deposition. Further details on these improvements are provided in the Supporting Information Section 2.1.

2.2 Reducing stringing

Stringing refers to the formation of unintended thin strands of thermoplastic between printed features, caused by residual oozing during the non-print travel of the print head. Even after the extrusion screw stops rotating, molten material can continue to ooze due to gravity and residual back pressure within the barrel. This effect is especially pronounced in soft, elastic materials and can lead to geometric distortions, internal voids, and ultimately leakage or reduced device performance. In FFF, stringing is typ-

ically mitigated through filament retraction; however, applying retraction to elastomers often introduces extrusion instability, buckling, or inconsistent flow, making it unreliable for printing compliant materials [24]. Another widely used strategy is reducing the nozzle temperature to increase melt viscosity. While effective in suppressing oozing, this approach simultaneously reduces the achievable volumetric flow rate and print speed, and can significantly weaken interlayer adhesion due to insufficient thermal bonding [46]. As a result, these process-based strategies typically suppress stringing at the expense of print stability, throughput, or structural integrity.

An alternative strategy is to suppress stringing through intrinsic material rheology rather than process-based mitigation [47, 48]. FGF enables this approach by allowing direct use of pelletized elastomers with widely varying viscoelastic properties. In this work, we find that materials combining high low-shear viscosity, strong shear-thinning behavior during extrusion, and predominantly elastic response at low deformation rates exhibit substantially reduced residual oozing, enabling clean, high-speed printing without compromising extrusion stability or interlayer adhesion.

3 Material selection

An ideal material for pellet-based extrusion should suppress oozing to minimize stringing while enabling sufficiently high extrusion flow rates to support fast printing. To investigate a materials selection strategy, we evaluated four thermoplastic elastomer (TPE) pellets, Filaflex 60A, Baiyu 30A, TF2ATL 22A, and TF5ATL 50A, which exhibited distinct printing behaviors. We note that Filaflex 60A is the commercial name of the material, while the manufacturer's datasheet specifies a Shore hardness of 63A.

All materials went through print parameter tuning and trial prints to assess basic printability and identify suitable nozzle temperatures. Filaflex 60A, a commonly used soft TPU with a recommended FFF printing temperature of 235 °C, exhibited severe oozing in the FGF system even at 180 °C and without active rotation of the extrusion screw, preventing further printing tests. The remaining three materials were printable and could be tuned to fabricate airtight structures. However, parts printed with Baiyu 30A exhibited weak interlayer adhesion, leading to leakage under sustained pneumatic pressurization. Increasing the print temperature improved bonding but simultaneously increased oozing. In contrast, TF2ATL 22A and TF5ATL 50A enabled stable printing with minimal stringing and no observable interlayer adhesion issues.

To compare quantitatively materials without relying on extensive print trials, we designed a set of extrusion and oozing tests combined with rheological characterization. For each material, the evaluation

temperature was selected based on its observed printing performance.

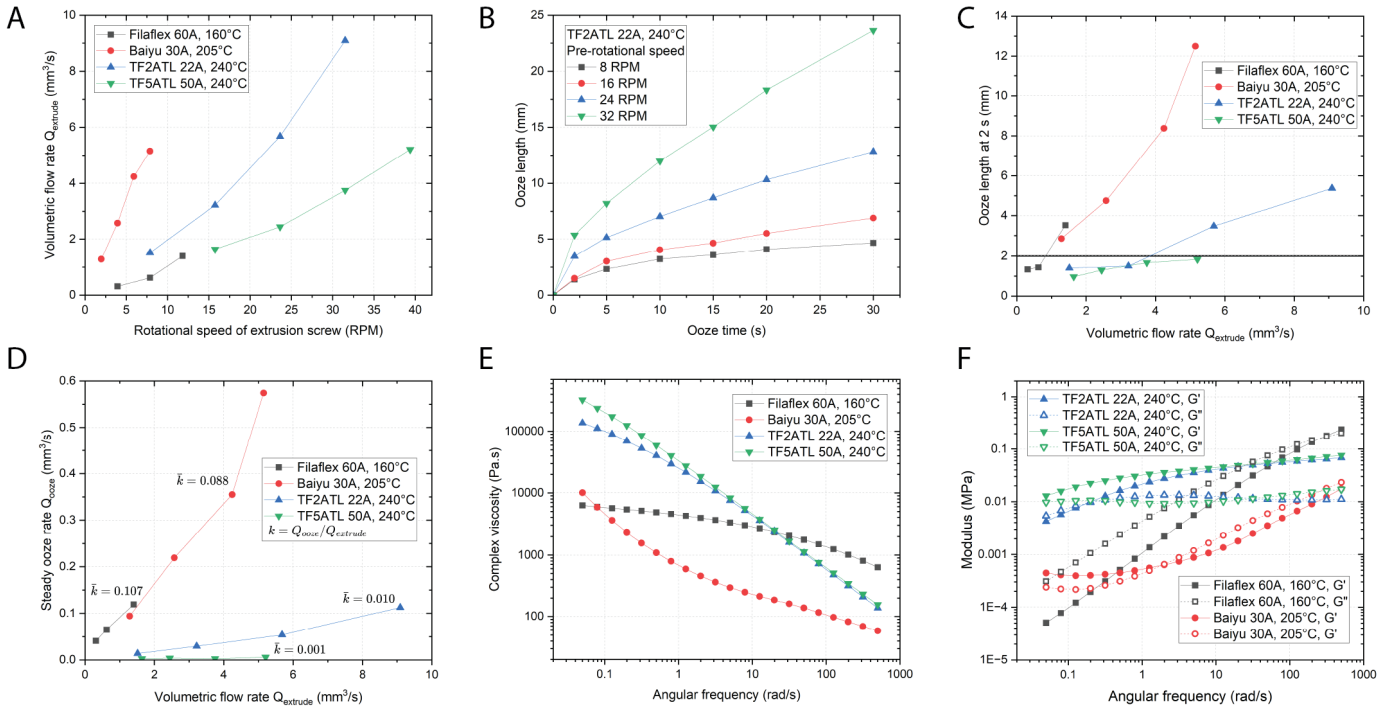

Figure 2: **Extrusion and rheology characterization of TPE pellets.** (A) Volumetric flow rate as a function of rotational speed of the extrusion screw for different pellets at their respective print temperatures. (B) Oozed length versus time for pellets with a Shore hardness of 22A at a temperature of 240 °C under different rotational speeds of the extrusion screw. (C) Oozed length after 2 seconds versus volumetric flow rate for different materials at their respective print temperatures, showing that at the same volumetric flow rate, the 22A and 50A material exhibits significantly less oozing than the other two materials. 2 mm ooze at 2s is chosen as the criterion for determining maximum extrusion flow rate. (D) Steady ooze rate as a function of extrusion rate, and k of each material is calculated as the average of $Q_{ooze}/Q_{extrude}$ of all measured flow rates. (E) Complex viscosity as a function of angular frequency for all four materials. (F) Storage modulus and loss modulus as a function of angular frequency for all four materials, showing the liquid-solid transition frequency (G'/G" crossover frequency) differences.

3.1 Extrusion and oozing tests

The extrusion test quantified the volumetric flow rate as a function of the rotational speed of the extrusion screw. For all materials, the extrusion flow rate increased with rotational speed (**Figure 2A**). The oozing test measured the length of extruded material as a function of time after stopping the rotation of the extrusion screw. The rotational speeds used in the oozing tests matched those in the extrusion tests, enabling direct comparison between extrusion and idle flow behavior. The oozed length-time profiles exhibited a common trend across materials: a high initial oozing rate immediately after stopping extrusion, followed by a gradual decrease and stabilization after several seconds (**Figure 2B**).

Plotting oozed length against the corresponding extrusion flow rate yielded a material-dependent oozing performance profile (**Figure 2C**). All materials exhibited increased oozing at higher extrusion rates,

Table 1: **Summary of extrusion, oozing, and rheological properties of the tested TPE pellets.** T_{nozzle} represents nozzle temperature. Q_{max} represents the maximum extrusion flow rate for which the corresponding oozed length remains below 2 mm within 2 s. $\bar{k}$ represents average of $Q_{ooze}/Q_{extrude}$. $\eta(0.05)$ represents low-shear viscosity at 0.05 rad/s. $\eta(500)$ represents high-shear viscosity at 500 rad/s. n represents shear thinning index. ω_c represents G'/G'' crossover frequency.

Material	T_{nozzle} (°C)	Q_{max} (mm^3/s)	$\bar{k}$	$\eta(0.05)$ (Pa·s)	$\eta(500)$ (Pa·s)	n	ω_c (rad/s)
Filaflex 60A	160	0.6	0.107	6273.47	630.92	0.645	280
Baiyu 30A	205	0.9*	0.088	10089.3	58.42	0.6556	> 500
TF2ATL 22A	240	3.2	0.010	137365	137.82	0.1332	0.17
TF5ATL 50A	240	5.2	0.001	324930	155.89	0.1344	< 0.05

$*$ Estimated by fitting a linear model of the ooze length-extrude flow data of Baiyu 30A

reflecting an inherent tradeoff between high throughput and low oozing. However, pronounced differences were observed across materials: at the same extrusion rate, TF2ATL 22A and TF5ATL 50A consistently exhibited lower oozing than Baiyu 30A and Filaflex 60A. For example, when a criterion of less than 2 mm oozed length within 2 s was applied, Baiyu 30A and Filaflex 60A were limited to extrusion rates below approximately 1 mm^3/s, whereas TF2ATL 22A and TF5ATL 50A supported extrusion rates of approximately 3.2 mm^3/s and 5.2 mm^3/s, respectively.

To facilitate direct comparison across materials and operating conditions, we introduce a normalized oozing metric $k = Q_{ooze}/Q_{extrude}$, which relates the oozing flow rate Q_{ooze} to the extrusion flow rate $Q_{extrude}$. While the oozed length measured at 2 s reflects the initial transient oozing behavior, the normalized metric k is calculated using the steady-state oozing rate obtained between 15 and 30 s after the rotation of the extrusion screw stopped. For each material, the average normalized oozing metric $\bar{k}$ is calculated. Using this definition, TF2ATL 22A exhibits an approximately one order of magnitude lower $\bar{k}$ value than the higher-oozing materials, while TF5ATL 50A exhibits an even lower $\bar{k}$, approaching a two orders of magnitude reduction (**Figure 2D**).

3.2 Rheological characterization

Oscillatory frequency sweeps were performed to characterize the complex viscosity η, storage modulus G', and loss modulus G'' of each material at the selected temperatures (see Experimental section for details). The angular frequency refers to the oscillatory deformation frequency applied in the rheometer and serves as a proxy for shear rate $\dot{\gamma}$ through the Cox–Merz relation. It is not directly related to the rotational speed of the extrusion screw in the FGF system. For reference, the apparent shear rate during extrusion can be estimated from the volumetric flow rate Q using $\dot{\gamma} \sim \frac{32Q}{\pi d_n^3}\frac{3n+1}{4n}$, where d_n is the nozzle diameter and n is the shear-thinning index [49]. Four rheological descriptors were extracted to interpret differences in oozing behavior: (i) high-shear viscosity, (ii) low-shear viscosity, (iii) shear-thinning index

n, and (iv) the G'/G'' crossover frequency (**Table 1**).

High-shear viscosity reflects resistance to flow during active extrusion and therefore influences achievable extrusion throughput, whereas low-shear viscosity characterizes resistance to flow after extrusion stops and is directly relevant to idle oozing. The shear-thinning index quantifies how rapidly viscosity increases as the shear rate decreases. Both low-oozing materials (TF2ATL 22A and TF5ATL 50A) exhibited higher low-shear viscosity and stronger shear-thinning behavior than the high-oozing materials (Filaflex 60A and Baiyu 30A), enabling suppression of residual flow without compromising extrusion throughput (**Figure 2E**).

The G'/G'' crossover frequency ω_c marks the transition where a polymer melt shifts from predominantly viscous ($G'' > G'$) to predominantly elastic ($G' > G''$), providing additional insight into viscoelastic behavior. TF5ATL 50A exhibited the lowest crossover frequency, corresponding to a more elastic melt response under low-shear conditions, consistent with its rapid decay of oozing after the rotation of the extrusion screw stops. In contrast, Filaflex 60A and Baiyu 30A exhibited high crossover frequencies, indicating more liquid-like behavior over a broad shear-rate range and a stronger dependence of oozing on extrusion rate (**Figure 2F**). These differences are consistent with the observed variations in the normalized oozing metric $\bar{k}$.

3.3 Material selection guideline

Based on these results, we propose a two-level material selection strategy for FGF. When a specific printer and material are available, extrusion and oozing tests can be used to construct an oozing performance profile (**Figure 2C, D**) that relates idle oozing behavior to extrusion flow rate, enabling selection of print speed based on an acceptable oozing threshold. In this study, printing with a print speed that corresponds to an oozed length of less than 2 mm within 2 s was found to enable clean printing without excessive stringing, supporting fabrication of airtight soft structures.

For general material screening, low oozing combined with high extrusion throughput is favored by a rheological profile characterized by low high-shear viscosity, high low-shear viscosity, strong shear-thinning behavior, and a low G'/G'' crossover frequency. The rheological values reported here provide reference points for evaluating candidate materials and illustrate how rheological state governs oozing behavior in pellet-based extrusion.

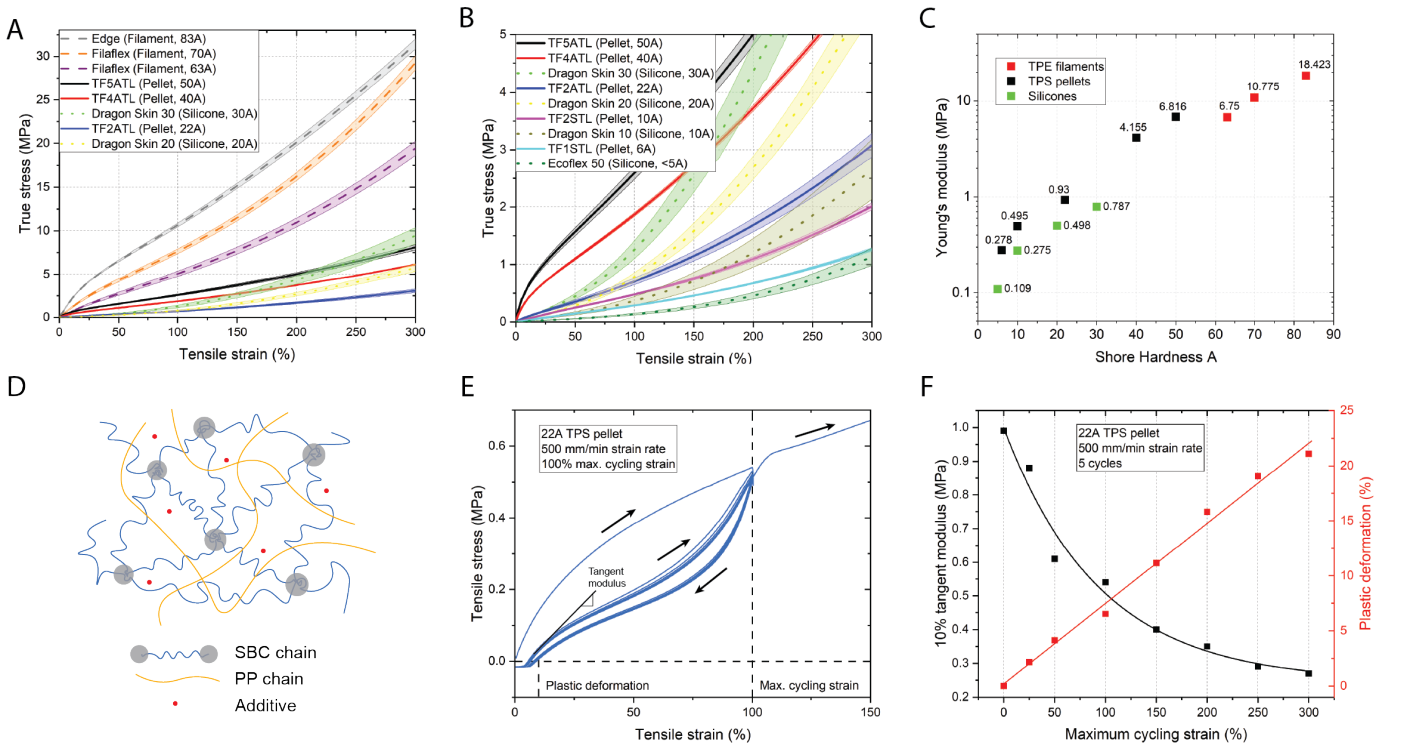

Figure 3: **Mechanical characterization of TPE filaments, TPS pellets, and silicone materials for soft structure fabrication.** (A) True stress–strain curves up to 300% strain, with shaded 95% confidence intervals from five tests. (B) Zoomed-in view highlighting stress-strain response of materials with lower Young's modulus. (C) Young's modulus versus Shore hardness, showing the correlation between stiffness and hardness. (D) Microstructure of an SBC–PP blend TPS material. PP is commonly incorporated into TPS formulations to tune elasticity and processability. (E) Representative tensile cycling test on 22A TPS pellets, illustrating loading–unloading behavior, tangent modulus, and plastic deformation. (F) Effect of maximum cycling strain on 10% tangent modulus and plastic deformation for 22A pellets.

4 Material characterization

To guide our material selection and better understand the behavior of printed structures, we characterized representative TPE filaments, TPS pellets, and silicone rubbers. Five dogbone specimens per material were prepared using FDM printing, FGF printing, and molding in accordance with ASTM D412 and tested under uniaxial tension. We converted the engineering strain to true strain to more accurately capture nonlinear behavior at low strain, and plotted stress-strain curves up to 300% strain along with 95% confidence intervals for each material (**Figure 3A**). Our results show that TPE filaments exhibit high stiffness and strain softening within the first 100% strain, reflecting their high initial modulus and limited extensibility. In contrast, TPS pellets displayed substantially lower stiffness. Softer pellets, particularly those with Shore hardness below 22A, exhibited low modulus and minimal initial softening, showing mechanical behavior comparable to commercial silicones (**Figure 3B**). The observed correlation between Young's modulus and Shore hardness confirms the general trend of increasing stiffness with Shore hardness and demonstrates the wider modulus range achievable with TPS pellets (**Figure 3C**).

Commercial TPS pellets contain not only styrenic block polymer (SBC) but also polypropylene (PP) (**Figure 3D**). PP helps tune the elasticity and processability of TPS materials but also contributes to a more pronounced Mullins effect, an irreversible stress-softening observed in elastomers after the first loading cycle. To evaluate elastic recovery and fatigue behavior, we conducted cyclic tensile tests on samples fabricated from 22A TPS pellets at a strain rate of 500 mm/min with incremental strain limits. The loading–unloading curve of the 22A material reveals a reduction in tangent modulus and the presence of permanent plastic deformation (**Figure 3E**). Most mechanical degradation occurs during the first cycle, after which subsequent cycles show more stable behavior (**Supporting Information, Figure S4**). Increasing the maximum strain leads to a monotonic rise in plastic deformation and a corresponding decrease in the 10% tangent modulus (**Figure 3F**).

5 Case study: Pellet printed pneumatic actuators

5.1 Mechanical characterization of pellet printed PneuNets

To evaluate the performance of soft devices fabricated via FGF, we designed, printed, and tested a pneumatic network (PneuNet) actuator using TPS pellets of varying Shore hardness. Actuation performance was evaluated by measuring the bending angle as a function of input pressure (**Figure 4A**) and comparing the results with silicone-molded and filament-printed PneuNet actuators (**Supporting Information, Figure S5**).

To assess long-term durability, we subjected the 22A actuator to continuous operation for up to 100,000 actuation cycles (**Figure 4B**). The pressure–bending relationship remained consistent throughout testing, showing minimal degradation in peak angle or response behavior. These results confirm that soft actuators fabricated via FGF maintain airtightness and mechanical integrity under extended use. A distinct change between the first and second cycles reflects the Mullins effect, which stabilizes thereafter and does not compromise long-term functionality. The Mullins effect observed in 3D-printed TPS structures can be viewed as a form of mechanical conditioning, during which the actuator reaches its steady-state performance.

We further examined the effect of extrusion flow rate on actuator performance (**Figure 4C**). Under-extrusion resulted in poor interlayer adhesion and leakage, while over-extrusion caused stringing and geometric distortion. By fine-tuning the flow rate, we achieved reproducible fabrication of airtight actuators with consistent bending behavior. However, Finite Element Analysis (FEA) aligned more closely

with the response of under-extruded actuators, suggesting that the over-extrusion typically used to ensure airtightness causes deviations between experimental and simulated performance.

We investigated the material-dependent mechanical response of pneumatic actuators by fabricating PneuNets using FGF with TPS pellets spanning Shore hardness values from 6A to 50A (**Figure 4D**). Under identical input pressures, softer materials produced significantly greater deformation due to their lower elastic modulus and higher compliance. In contrast, a PneuNet printed via FFF using a commer-

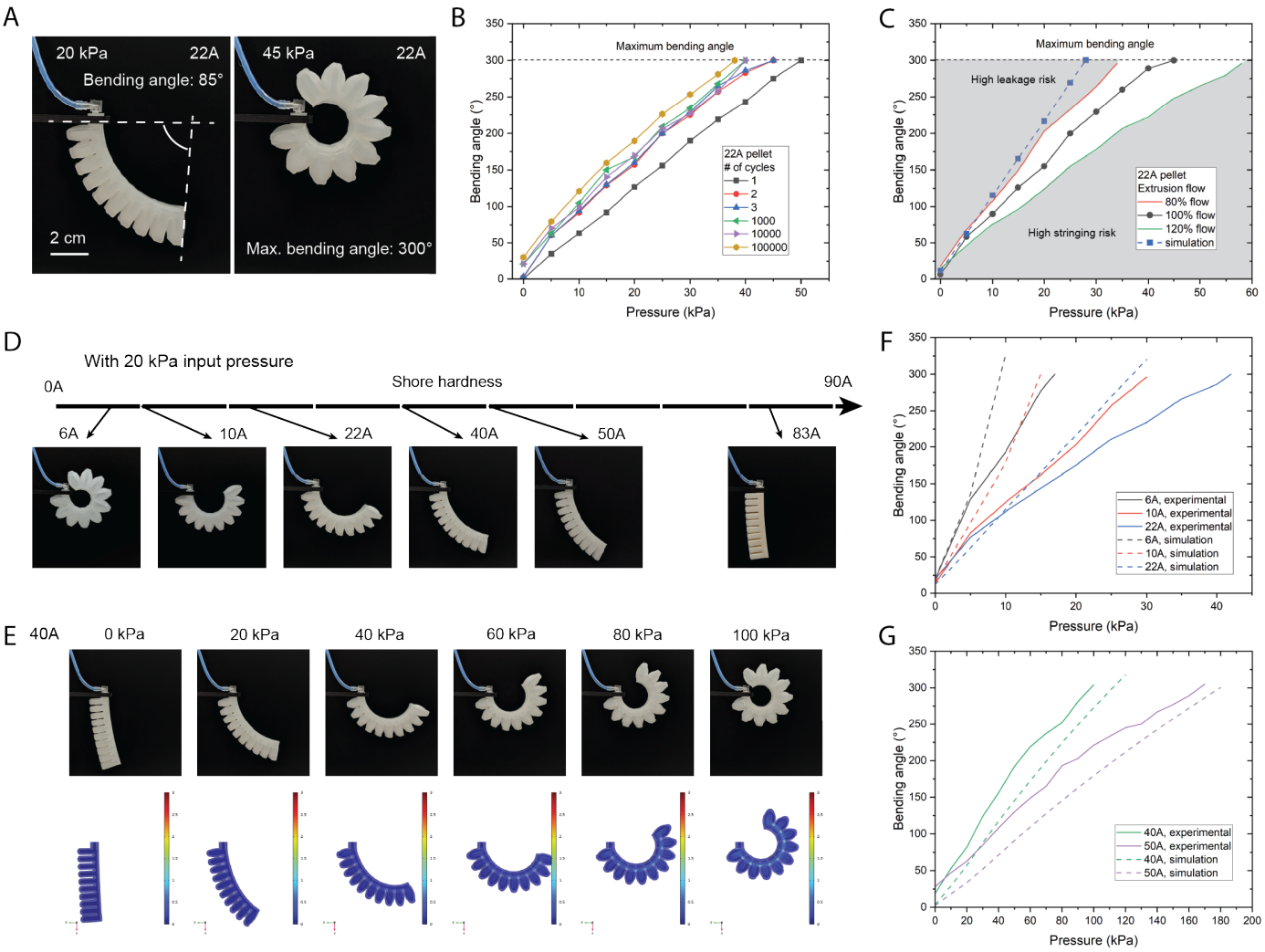

Figure 4: **Characterization of soft actuators printed with TPS pellets using FGF.** (A) PneuNet actuator fabricated from 22A pellets, illustrating bending angles of 85 °and 300 °at maximum deformation. (B) Bending angle as a function of pressure measured over 1–100,000 actuation cycles, demonstrating stable and repeatable actuator performance. (C) Effect of extrusion flow rate on actuator bending behavior; shaded regions denote operating conditions associated with leakage and stringing. The flow percentage indicates the relative setting with respect to the recommended flow rate for the 22A pellet and does not represent the absolute volumetric flow rate. (D) Comparison of actuator bending at 20 kPa for materials with varying Shore hardness, illustrating the influence of material stiffness on deformation performance. (E) Experimental and simulated deformation profiles of a 40A actuator under increasing pressure, highlighting the agreement between measured and predicted bending behavior. (F) Bending angle as a function of pressure for 6A, 10A, and 22A actuators, showing reduced experimental bending compared to simulations due to over-extrusion effects during fabrication. (G) Comparison of bending angles for 40A and 50A actuators, with discrepancies between experimental and simulated results attributed to the Mullins effect and material stress softening.

cial TPU filament (Ninjaflex Edge, 83A) exhibited minimal bending. This result highlights the importance of 3D printable materials with Shore hardness comparable to silicones, which here enable large deformations in soft pneumatic actuators.

5.2 Numerical simulation of PneuNet bending behaviors

To gain deeper insight into actuator performance and evaluate the accuracy of our simulations, we conducted FEA using material models calibrated with uniaxial tensile test data. For each material, a hyperelastic constitutive model was fitted to capture nonlinear deformation behavior, and the pressurization-induced response of the PneuNet actuators was simulated. The resulting simulated deformations were then compared with experimental measurements to evaluate the fidelity of the model.

The simulated deformation profiles showed strong agreement with the experimentally observed bending shapes, confirming that the fitted material models accurately captured the overall deformation behavior (**Figure 4E**). However, systematic discrepancies were evident in the pressure–bending angle relationships across different materials.

For actuators fabricated from 6A, 10A, and 22A TPS pellets, the experimentally measured bending angles were consistently lower than those predicted by the numerical model (**Figure 4F**). This discrepancy is likely due to over-extrusion during printing, which increased wall thickness and overall stiffness—factors not represented in the idealized numerical model. In contrast, actuators printed with 40A and 50A pellets exhibited bending angles exceeding the simulated predictions (**Figure 4G**). This deviation is attributed to the Mullins effect, a stress-softening phenomenon not captured by the material models, which becomes more pronounced in stiffer elastomers subjected to large strains.

These comparisons highlight the importance of studying fabrication-induced variability and time-dependent viscoelastic effects to improve the predictive accuracy of computational models for soft pneumatic actuators.

6 Demonstrations

6.1 Soft robotic hand

We designed, fabricated, and tested a fully soft robotic hand to demonstrate the capability of FGF to produce complex, integrated fluidic devices. Printing the hand with 22A pellets required 20 hours and 40 minutes (**Movie S2**). The hand consists of five fingers, each containing three independent embed-

ded pneumatic chambers connected through integrated fluidic pathways (**Figure 5A**). The structure was printed monolithically, without any post-processing or assembly. Thin outer walls (1.5 mm, three perimeters) and a 50% gyroid infill were used to balance compliance and airtightness (**Figure 5B**). All inflatable chambers connect to internal channels that merge at the back of the hand within a compact routing manifold, allowing 15 individual tubes to deliver pressurized air to each chamber for actuation (**Figure 5C**). Sequential actuation of these chambers enables coordinated bending across the finger segments, culminating in a full grasping configuration (**Figure 5D**). The robotic hand successfully grasped objects of varying sizes and geometries (**Figure 5E**, **Movie S3**), demonstrating the effectiveness of FGF in fabricating functional, monolithic soft robotic systems with intricate internal channel networks.

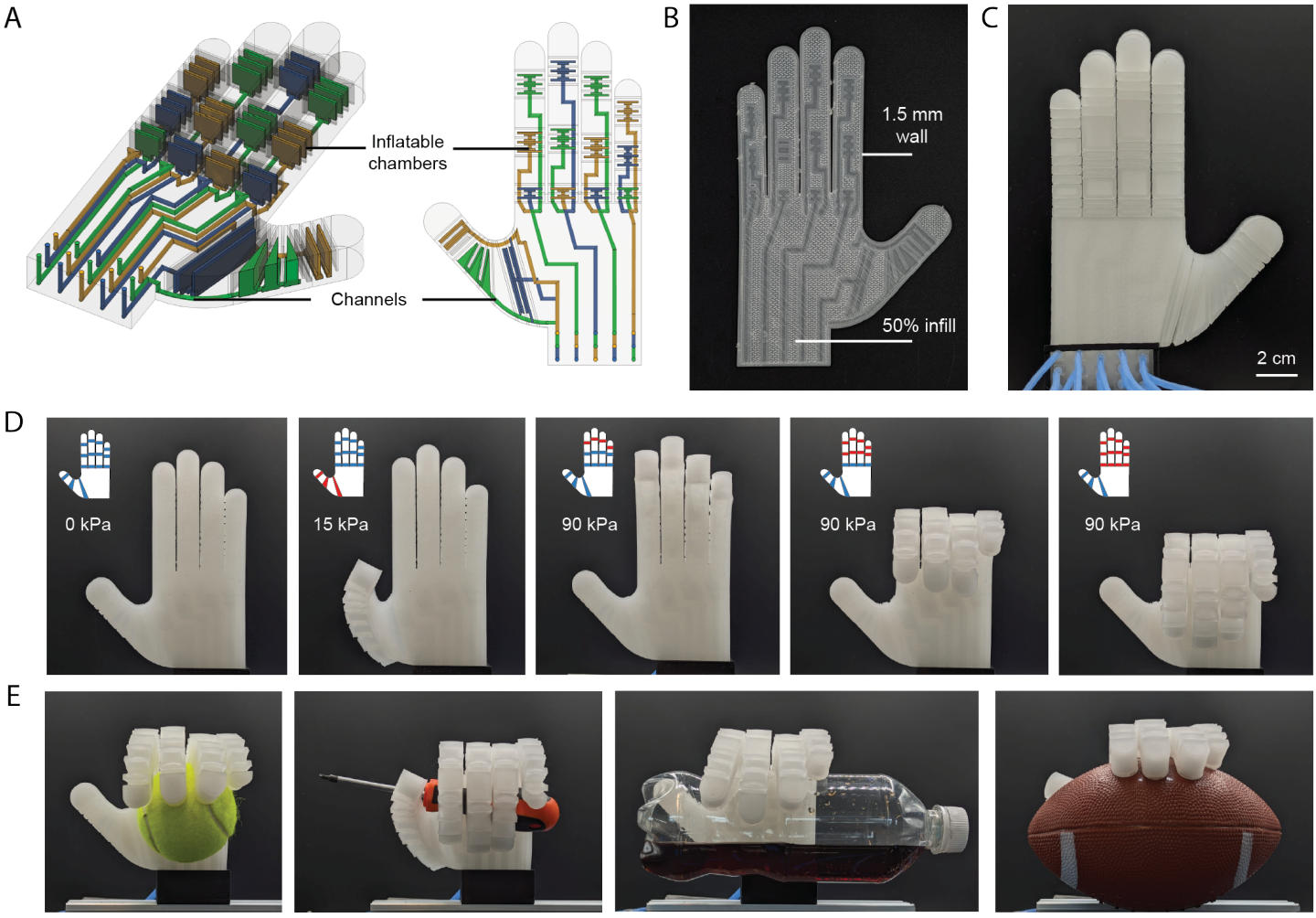

Figure 5: **Robotic hand demonstrating reliable FGF printing of a complex fluidic device.** (A) Semi-transparent CAD rendering of the hand design, with blue, yellow, and green regions indicating internal channels and inflatable chambers. (B) Close-up image of the printed hand at a 3 mm layer height, showing thin-wall structures, internal channels, and 50% gyroid infill. (C) Image of the backside of the printed hand. (D) Actuation sequence illustrating the transition from the extended to fully grasping state through sequential activation of chambers in the fingers and thumb. Hand schematics in the top left corner indicate actuator status, with red denoting actuated and blue representing unactuated chambers. (E) Demonstration of the robotic hand grasping a variety of everyday objects.

6.2 Soft robotic fish

We fabricated a soft robotic fish using FGF to evaluate the airtightness and structural integrity of monolithically printed components for underwater applications. The design was intentionally developed to demonstrate the feasibility of printing tall, geometrically complex structures with extended bridges and overhangs. Such features remain difficult to achieve with conventional FDM-fabricated soft systems, which are generally constrained to low-profile architectures. The robot consists of three sections: head, body, and tail (**Figure 6A**). They can be printed using 22A TPS either as separate parts assembled post-printing or as a single monolithic structure with support material.

Monolithic printing with support material required 17 hours and 9 minutes (**Figure 6B**, **Movie S4**). The body section houses all pneumatic chambers, featuring 2 mm-thick outer walls (four perimeters) and bridges exceeding 10 mm in length. A central spinal structure was added to distribute airflow and support bridges during printing. To enhance print reliability, all first-layer bridges were oriented along their shorter span, and travel speed was reduced to 100 mm/s to limit vibration, especially when print-

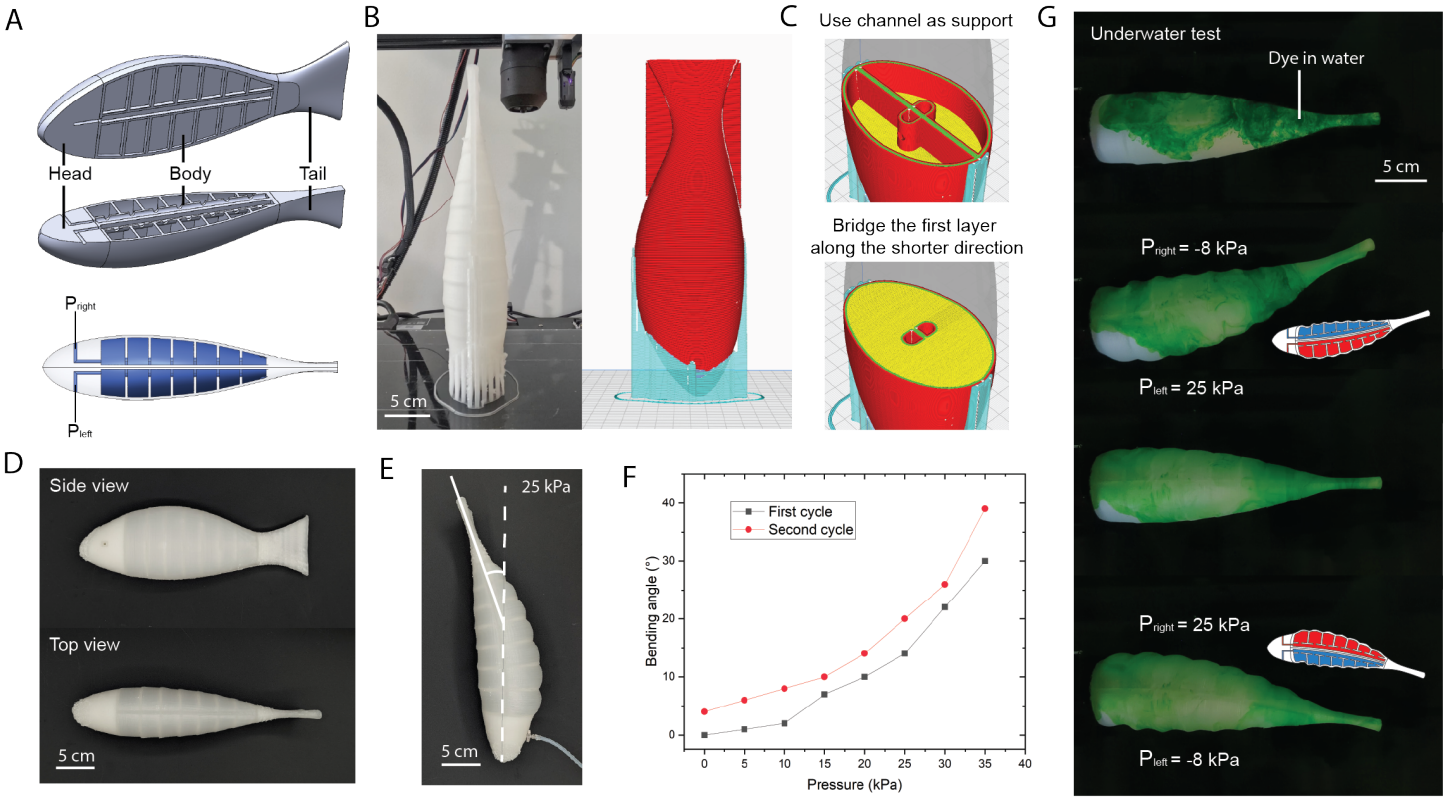

Figure 6: **Robot fish demonstrating airtight print for underwater applications.** (A) Cross-sectional CAD view of the robotic fish design and schematic of the two-chamber actuation principle. (B) Slicer view (right image) of the fish model (blue regions indicate support material) and photograph of the printed part (left image) in its final state. (C) Design principle for long bridges. (D) Photographs of the printed fish from side and top views. (E) Photograph of the robotic fish bending during actuation of its left chamber (right side from the viewer's perspective) at 25 kPa, with the bending angle measurement indicated. (F) Bending angle as a function of input pressure over two actuation cycles. (G) Underwater images of the actuated robotic fish demonstrating full airtightness and periodic tail-swinging motion.

ing taller sections (**Figure 6C**). The actuator architecture comprises two independent pneumatic chambers located on the left and right sides of the body. Differential pressurization of these chambers induces lateral bending of the body and tail. The bending angle at identical input pressures increased after the first activation cycle, consistent with Mullins-type stress softening (**Figure 6E, F**). During underwater testing, the robotic fish remained airtight throughout repeated actuation cycles (**Figure 6G**, **Movie S5**).

6.3 Wearable pressure cuff

We demonstrated the fabrication of wearable pneumatic devices by 3D printing a soft pressure cuff with embedded inflatable chambers using 50A TPS pellets. The design featured a single-layer thin inner wall and a thicker outer wall, with interconnected chambers enabling uniform pressurization (**Figure 7A**). The cuff was printed monolithically in 9 hours and 26 minutes. Upon inflation through a single inlet, the asymmetric wall geometry caused the thinner inner wall to bulge inward, generating radial compression around the limb (**Figure 7B**). The geometry was optimized to operate within standard blood pressure ranges (11.3–17.3 kPa), providing a balance between compliance and stiffness. Compared to the 22A pellets used in other demonstrations, the 50A material offered improved mechanical stability while maintaining sensitivity to modest pressure variations. Despite its thin-wall design, the cuff remained fully airtight, underscoring the reliability of the FGF extrusion process. When applied to the upper arm, the device generated uniform radial pressure and enabled systolic pressure measurement via an external pressure sensor (**Figure 7C,D**). The cuff maintained stable internal pressure across repeated actuation cy-

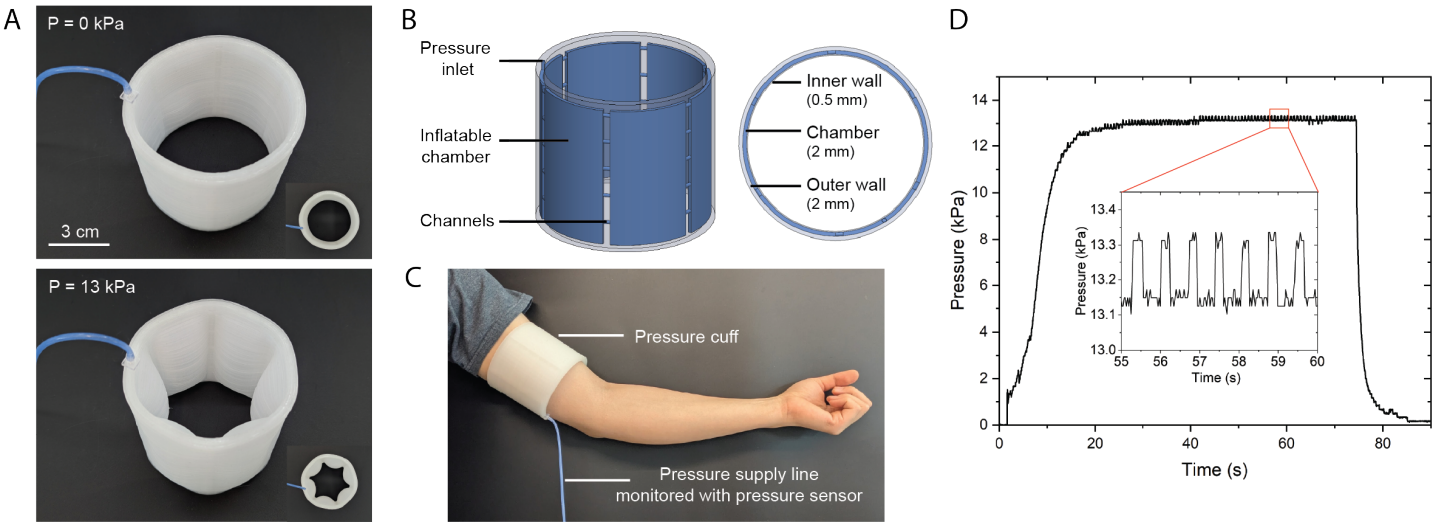

Figure 7: **Pressure cuff demonstrating wearable applications.** (A) Photographs of the printed cuff in unpressurized (0 kPa) and pressurized (13 kPa) states. (B) CAD model and cross-sectional view of the pressure cuff, with blue regions showing the internal inflatable chambers and channels. (C) Demonstration of the cuff worn on an arm. (D) Pressure profile during inflation, with inset showing high-frequency pressure fluctuations from the heartbeat.

cles, and the presence of high-frequency pressure oscillations in the recorded signal confirmed both the airtightness of the chambers and the mechanical responsiveness of the structure to dynamic loading conditions (**Figure 7E**).

7 Discussion

FGF provides access to a vast and largely untapped library of thermoplastic materials from the established polymer industry, including hydrophobic, conductive, biodegradable, and recycled formulations. This versatility enables designers to expand the functional scope of 3D-printed soft devices by tailoring material properties to specific application requirements. By facilitating the use of diverse thermoplastics with tunable mechanical, electrical, and chemical characteristics, FGF supports application-specific customization and scalable manufacturing, enabling new designs and use cases beyond the reach of traditional filament-based approaches.

Each new material, however, necessitates dedicated evaluation of its printability and the performance of the resulting structures. The present work introduces a systematic framework and workflow for tuning and characterizing materials, establishing a foundation for future exploration. To further broaden the accessible material space, it will be essential to identify and define material requirements suited for FGF, such as high viscosity and pronounced shear-thinning behavior to minimize oozing and enhance print fidelity. These criteria can guide the formulation of new thermoplastic blends specifically optimized for the rapid fabrication of high-quality soft devices.

Looking ahead, enabling multimaterial FGF will make it possible to fabricate complex, gradient, or functionally segmented soft robots within a single print, combining materials of similar chemistry but differing stiffness, conductivity, or permeability in one monolithic structure. The insertion of supplementary materials into the pellet hopper to enable the extrusion of functionalized materials is also feasible. Multimaterial FGF will also address current limitations in printing overhangs and bridges by using dissolvable or sacrificial support materials, enabling more advanced designs and improved performance in next-generation soft robotic systems.

Beyond fabrication, we believe the stress-softening associated with the Mullins effect can be deliberately exploited as a design feature, where the initial inelastic deformation is used to program application-specific mechanical responses.

8 Conclusion

This work presents a comprehensive experimental framework for pellet-based fabrication of soft devices, combining mechanical characterization of thermoplastic styrenic block copolymers, quantification of Mullins-effect-induced softening, and long-term evaluation of pneumatic actuator durability and bending performance supported by finite element simulations. Across all tested materials, pronounced first-cycle softening and strain-dependent stress evolution highlight the importance of initial activation and material selection for achieving stable, repeatable mechanical response in soft thermoplastic systems. Airtightness and functional reliability were validated through the fabrication of diverse monolithically printed devices, including a soft robotic hand, an underwater robotic fish, and a wearable pressure cuff.

Beyond demonstrating device performance, this study establishes a materials-selection framework for fused granulate fabrication of soft systems. Material-specific oozing performance profiles can be constructed using extrusion and oozing tests, enabling determination of the maximum printable flow rate, and thus print speed, that maintains airtight fabrication by limiting the oozed length to less than 2 mm within 2 s, corresponding to an average initial oozing rate below approximately 1 mm/s. By linking oozing behavior to key rheological descriptors, this analysis highlights the importance of high low-shear viscosity, strong shear-thinning behavior, and a low G'/G'' crossover frequency for effective oozing control. Together, these results provide practical guidelines for selecting commercially available pellets that support high-throughput printing while suppressing residual oozing. This materials-informed approach shifts oozing control away from trial-and-error process turning toward predictive material selection, reducing reliance on retraction strategies or hardware modification.

Together, these results position FGF as a robust and versatile manufacturing strategy for both rapid prototyping and scalable production of large, complex soft devices. Soft materials within the Shore 00 and ultra-soft Shore A ranges, previously fabricated predominantly through soft lithography, can now be digitally manufactured using FGF with comparable mechanical performance. By enabling reliable extrusion of silicone-soft thermoplastics at substantially higher throughput than conventional FFF systems, FGF expands the accessible design space for soft robotics and wearable devices while maintaining compatibility with commercially available materials and printers.

9 Experimental Section

Pellet printer setup: We used an Ender 3 Pro Plus FFF printer as the base platform. The standard filament extruder was replaced with a Direct3D pellet extruder. To improve feeding reliability, the Direct3D pellet hopper was redesigned with steeper wall angles to enhance gravitational flow, and its internal surfaces were coated with PTFE to reduce wall friction and prevent pellet bridging. A Raspberry Pi 4 running Klipper firmware was integrated for direct process control, and slicing was performed using Cura (v5.8.1).

Material preparation: All compliant raw materials used in this study were commercially sourced (**Supporting Information, Table S1**). The TPS pellets selected for mechanical characterization and printing were obtained from Kraiburg TPE GmbH in Germany. To prevent moisture-related defects such as cavity formation due to water evaporation at the print nozzle, all filaments and pellets were pre-dried in a filament dryer (Sunlu S4) at 60°C for 6 hours and subsequently stored in a dry cabinet (Manncorp Ultra-Dry 790V) maintained below 5% relative humidity until use.

Extrusion test: For the extrusion flow rate test, the nozzle was preheated to the target temperature, after which the extrusion screw was rotated at a fixed speed for a set duration sufficient to collect a measurable amount of extruded material. Using the measured mass m, extrusion time t, and material density ρ, the volumetric flow rate was calculated as $Q_{extrude} = m/\rho t$. For the oozing test, the extrusion screw was rotated for 60 s, after which the nozzle was manually wiped immediately upon stopping. The subsequent oozing process was recorded on video, and the length of the oozed filament l_{ooze} was later measured as a function of time t_{ooze}. Assuming that the oozed filament retained an approximately circular cross-section with a diameter equal to the nozzle diameter d, the oozing rate can then be calculated as $Q_{\mathrm{ooze}} = \frac{\pi d^2}{4} \frac{\Delta l_{\mathrm{ooze}}}{\Delta t_{\mathrm{ooze}}}$

Rheology experiment: Rheological properties were measured using a TA Instruments HR20 rheometer equipped with an environmental test chamber and a 25 mm parallel-plate geometry. Steady shear measurements at high shear rates were not feasible because the melts exhibited edge fracture and ejection from the plates. Therefore, oscillatory frequency sweeps were performed, and the shear-rate–dependent viscosity was estimated using the Cox–Merz rule [50], which provides a stable and repeatable approximation for highly deformable polymer melts. For each material, a strain sweep at 100 rad/s was first performed to determine the linear viscoelastic (LVE) region. A strain amplitude of 1%, well within the LVE regime for all tested materials, was then used for oscillatory frequency sweeps. Frequency sweeps were

conducted from 500 rad/s down to 0.05 rad/s, although in some cases measurements were terminated early due to material oozing from the plates. Prior to testing, all samples were dehydrated at 60°C for 6 hours, and before each measurement, samples were preheated to the target temperature for 180 s to ensure thermal equilibrium. The shear-thinning index n was obtained by fitting a power-law model to the viscosity data derived from the frequency sweeps. To ensure consistency across materials, the fitting was restricted to the frequency range of 10-500 rad/s, where apparent shear-thinning behavior exhibited an approximately constant slope for all materials.

Tensile test experiment: All test bars were fabricated according to the ASTM D412 Type C standard with a thickness of 3 mm. TPE test bars were printed using either FFF or FGF, while silicone test bars were cast in molds fabricated via FFF. Tensile tests were conducted using a universal testing machine (Instron 68TM-50) equipped with a 500 N load cell. Following the standard, a strain rate of 500 mm/min was applied during testing. For each specimen, the initial clamp distance, width, and thickness were recorded to calculate strain and cross-sectional area. A prestress of 0.5 N was applied for most samples, while softer materials with Shore hardness below 10 A were tested using a reduced prestress of 0.1 N.
For cycling tests, the Instron 68TM-50 was programmed to pull the test bars between 0% strain and a specified maximum strain (varied depending on test conditions) for five consecutive cycles, followed by a final pull to a predefined maximum extension. All cyclic tests were performed at a strain rate of 500 mm/min, consistent with the uniaxial tensile tests.

PneuNet test setup: Each PneuNet was fabricated using the same print parameters as those employed for the mechanical test bars to ensure experimental consistency. The actuators were mounted on a fixed test frame against a black background, and images were captured at discrete pressure intervals. Bending angles were quantified from these images through post-processing. For cyclic testing, the same image-based analysis was applied to selected cycles. Actuation was controlled by an Arduino Mega, which applied 35 kPa at 5-second intervals to achieve near-complete bending in each cycle.

Simulation setup: The bending behavior of the pneumatic actuator was analyzed using COMSOL Multiphysics 6.2. A 3D stationary study was performed with a mesh defined in normal mode and element sizes ranging from 1 to 3 mm. A fixed boundary condition was applied to the surface containing the inlet connection. To capture mechanical interactions under high pressure, contact pairs were defined between adjacent chambers using a penalty factor of 1. Gravity was included in the vertical direction to replicate experimental conditions. Internal pressurization was simulated by applying a boundary load to the inner walls of the actuator. The bending angle was quantified by extracting the normal vector com-

ponents (n_x and n_y) from the distal surface of the actuator.

Material behavior was modeled using a third-order Ogden hyperelastic model (**Supporting Information, Section 7**). The model parameters for each material were fitted to true stress–strain data obtained from uniaxial tensile tests.

Demonstration setup: The robotic hand comprises 15 individually controlled pneumatic actuators. Each actuator was connected to a 12V solenoid valve (0520F), driven by a MOSFET driver module (YYNMOS-4) and controlled using an Arduino Mega 2560. The actuators in the index, middle, ring, and pinky fingers were operated at a uniform pressure of 90 kPa, while the thumb actuators were driven at a lower pressure of 15 kPa.

The robotic fish contains two internal pneumatic chambers. To maximize bending, pressure was applied to one chamber while a vacuum was simultaneously applied to the other. This differential actuation utilized four solenoid valves, two supplying positive pressure and two supplying vacuum, to achieve bending through controlled asymmetric pressurization. Both positive and negative pressures were generated by a 12V pump (SC3802PM-A). For underwater testing, the head of the robotic fish was removed to simplify fixture mounting and ensure stable positioning during actuation (**Movie S5, Supporting Information Figure S6**).

In the pressure sleeve, all chambers were connected to a single pneumatic line to enable single-input control. A pressure regulator (AFR2000) was used to limit the maximum supply pressure, and airflow was modulated by using tubing with a narrow inner diameter of 1.5 mm. Internal pressure was measured using a piezoresistive pressure sensor (XGZP6847A500KPG) connected to an analog-to-digital converter (ADS1115).

Supporting Information

Supporting Information is available from the Wiley Online Library or from the author.

Acknowledgements

We thank Josef Neuer of Kraiburg TPE GmbH in Germany for his support in guiding the material selection process. We also thank Professor Robert White and Souleymane Cissokho for providing access to the water tank used in the robotic fish experiments. This research was funded by the National Science Foundation (NSF) under award number 2512999.

References

[1] J. Fang, Y. Zhuang, K. Liu et al., "A Shift from Efficiency to Adaptability: Recent Progress in Biomimetic Interactive Soft Robotics in Wet Environments", *Advanced Science* **2022**, *9*, 8 2104347.

[2] M. M. Duran, G. Moro, Y. Zhang, A. Islam, "3D printing of silicone and polyurethane elastomers for medical device application: A review", *Advances in Industrial and Manufacturing Engineering* **2023**, *7* 100125.

[3] P. Polygerinos, Z. Wang, K. C. Galloway, R. J. Wood, C. J. Walsh, "Soft robotic glove for combined assistance and at-home rehabilitation", *Robotics and Autonomous Systems* **2015**, *73* 135.

[4] C. Aygül, C. Güven, S. A. Frunzi, B. J. Katz, M. P. Nemitz, "A framework for soft mechanism driven robots", *Nature Communications* **2025**, *16*, 1 1426.

[5] J. Hughes, U. Culha, F. Giardina, F. Guenther, A. Rosendo, F. Iida, "Soft Manipulators and Grippers: A Review", *Frontiers in Robotics and AI* **2016**, *3*.

[6] P. Polygerinos, N. Correll, S. A. Morin et al., "Soft Robotics: Review of Fluid-Driven Intrinsically Soft Devices; Manufacturing, Sensing, Control, and Applications in Human-Robot Interaction", *Advanced Engineering Materials* **2017**, *19*, 12 1700016.

[7] M. T. Tolley, R. F. Shepherd, B. Mosadegh et al., "A Resilient, Untethered Soft Robot", *Soft Robotics* **2014**, *1*, 3 213.

[8] R. Baines, S. K. Patiballa, J. Booth et al., "Multi-environment robotic transitions through adaptive morphogenesis", *Nature* **2022**, *610*, 7931 283.

[9] S. Kendre, G. Teran, L. Whiteside et al., "Printable Flexible Robots for Remote Learning", In *ASEE-NE 2022 Proceedings*. ASEE Conferences, Wentworth Institute of Technology, Massachusetts, **2022** 42267.

[10] P. Rothemund, A. Ainla, L. Belding et al., "A soft, bistable valve for autonomous control of soft actuators", *Science Robotics* **2018**, *3*, 16 eaar7986.

[11] S. Jain, S. Dontu, J. E. M. Teoh, P. V. Y. Alvarado, "A Multimodal, Reconfigurable Workspace Soft Gripper for Advanced Grasping Tasks", *Soft Robotics* **2023**, *10*, 3 527.

[12] T. J. Wallin, J. Pikul, R. F. Shepherd, "3D printing of soft robotic systems", *Nature Reviews Materials* **2018**, *3*, 6 84.

[13] H. Dong, T. Weng, K. Zheng, H. Sun, B. Chen, "Review: Application of 3D Printing Technology in Soft Robots", *3D Printing and Additive Manufacturing* **2024**, *11*, 3 954.

[14] L. Zhou, J. Fu, Y. He, "A Review of 3D Printing Technologies for Soft Polymer Materials", *Advanced Functional Materials* **2020**, *30*, 28 2000187.

[15] C. Tawk, R. Mutlu, G. Alici, "A 3D Printed Modular Soft Gripper Integrated With Metamaterials for Conformal Grasping", *Frontiers in Robotics and AI* **2022**, *8*.

[16] B. A. W. Keong, R. Y. C. Hua, "A Novel Fold-Based Design Approach toward Printable Soft Robotics Using Flexible 3D Printing Materials", *Advanced Materials Technologies* **2018**, *3*, 2 1700172.

[17] P. D. S. H. Gunawardane, P. Cheung, H. Zhou, G. Alici, C. W. De Silva, M. Chiao, "A Versatile 3D-Printable Soft Pneumatic Actuator Design for Multi-Functional Applications in Soft Robotics", *Soft Robotics* **2024**, *11*, 4 709.

[18] H. K. Yap, H. Y. Ng, C.-H. Yeow, "High-Force Soft Printable Pneumatics for Soft Robotic Applications", *Soft Robotics* **2016**, *3*, 3 144.

[19] T. Hainsworth, L. Smith, S. Alexander, R. MacCurdy, "A Fabrication Free, 3D Printed, Multi-Material, Self-Sensing Soft Actuator", *IEEE Robotics and Automation Letters* **2020**, *5*, 3 4118.

[20] J. Guo, Z. Li, J.-H. Low et al., "Kirigami-Inspired 3D Printable Soft Pneumatic Actuators with Multiple Deformation Modes for Soft Robotic Applications", *Soft Robotics* **2023**, *10*, 4 737.

[21] S. Conrad, J. Teichmann, P. Auth et al., "3D-printed digital pneumatic logic for the control of soft robotic actuators", *Science Robotics* **2024**, *9*, 86 eadh4060.

[22] Y. Zhai, A. De Boer, J. Yan et al., "Desktop fabrication of monolithic soft robotic devices with embedded fluidic control circuits", *Science Robotics* **2023**, *8*, 79 eadg3792.

[23] S. V. Kendre, C. Aygül, C. S. Page, L. Wang, M. P. Nemitz, "FDM-Printed CMOS Logic Gates from Flexing Beam Mechanisms for the Control of Soft Robotic Systems", *Advanced Intelligent Systems* **2025**, *7*, 2 2400468.

[24] Y. Wu, Z. Dai, H. Liu, L. Wang, M. P. Nemitz, "Vision-based FDM Printing for Fabricating Airtight Soft Actuators", In *2024 IEEE 7th International Conference on Soft Robotics (RoboSoft)*. **2024** 249–254, ISSN: 2769-4534.

[25] A. Hamidi, Y. Tadesse, "3D printing of very soft elastomer and sacrificial carbohydrate glass/elastomer structures for robotic applications", *Materials & Design* **2020**, *187* 108324.

[26] J. Li, S. Wu, W. Zhang, K. Ma, G. Jin, "3D Printing of Silicone Elastomers for Soft Actuators", *Actuators* **2022**, *11*, 7 200.

[27] H. Li, H. Bai, Z. Wang, Y. Tan, Y. Tang, "Soft bioinspired pneumatic actuator for adaptive grasping based on direct ink writing method", *Sensors and Actuators A: Physical* **2024**, *367* 115041.

[28] J. Plott, A. Shih, "The extrusion-based additive manufacturing of moisture-cured silicone elastomer with minimal void for pneumatic actuators", *Additive Manufacturing* **2017**, *17* 1.

[29] M. Schaffner, J. A. Faber, L. Pianegonda, P. A. Rühs, F. Coulter, A. R. Studart, "3D printing of robotic soft actuators with programmable bioinspired architectures", *Nature Communications* **2018**, *9*, 1 878.

[30] M. Wehner, R. L. Truby, D. J. Fitzgerald et al., "An integrated design and fabrication strategy for entirely soft, autonomous robots", *Nature* **2016**, *536*, 7617 451–455.

[31] D. K. Patel, A. H. Sakhaei, M. Layani, B. Zhang, Q. Ge, S. Magdassi, "Highly Stretchable and UV Curable Elastomers for Digital Light Processing Based 3D Printing", *Advanced Materials* **2017**, *29*, 15 1606000.

[32] T. J. K. Buchner, S. Rogler, S. Weirich et al., "Vision-controlled jetting for composite systems and robots", *Nature* **2023**, *623*, 7987 522.

[33] H. Matusik, C. Liu, D. Rus, "Directly 3D Printed, Pneumatically Actuated Multi-Material Robotic Hand", In *2024 IEEE International Conference on Robotics and Automation (ICRA)*. **2024** 2986–2992, URL `https://ieeexplore.ieee.org/document/10610016/mediamedia`.

[34] A. V. Nielsen, M. J. Beauchamp, G. P. Nordin, A. T. Woolley, "3D Printed Microfluidics", *Annual Review of Analytical Chemistry* **2020**, *13*, 1 45.

[35] K. Yamagishi, R. Karyappa, T. Ching, M. Hashimoto, "Direct ink writing of silicone elastomers to fabricate microfluidic devices and soft robots", *MRS Communications* **2024**, *14*, 5 846.

[36] M. Gepner, J. Mack, A. A. Stokes, "A standardized platform for translational advances in fluidic soft systems", *Device* **2025**, 100800.

[37] F. Pignatelli, G. Percoco, "An application- and market-oriented review on large format additive manufacturing, focusing on polymer pellet-based 3D printing", *Progress in Additive Manufacturing* **2022**, *7*, 6 1363.

[38] J. M. Justino Netto, H. T. Idogava, L. E. Frezzatto Santos, Z. d. C. Silveira, P. Romio, J. L. Alves, "Screw-assisted 3D printing with granulated materials: a systematic review", *The International Journal of Advanced Manufacturing Technology* **2021**, *115*, 9 2711.

[39] A. Georgopoulou, L. Egloff, B. Vanderborght, F. Clemens, "A Sensorized Soft Pneumatic Actuator Fabricated with Extrusion-Based Additive Manufacturing", *Actuators* **2021**, *10*, 5 102.

[40] S. Singamneni, M. P. Behera, D. Truong, M. J. Le Guen, E. Macrae, K. Pickering, "Direct extrusion 3D printing for a softer PLA-based bio-polymer composite in pellet form", *Journal of Materials Research and Technology* **2021**, *15* 936.

[41] M. A. H. Khondoker, D. Sameoto, "Direct coupling of fixed screw extruders using flexible heated hoses for FDM printing of extremely soft thermoplastic elastomers", *Progress in Additive Manufacturing* **2019**, *4*, 3 197.

[42] N. Willemstein, H. Van Der Kooij, A. Sadeghi, "3D-Printed Soft Proprioceptive Graded Porous Actuators with Strain Estimation by System Identification", *Advanced Intelligent Systems* **2024**, *6*, 9 2300890.

[43] A. Georgopoulou, S. Hamelryckx, K. Junge et al., "A multi-material robotic finger with integrated proprioceptive and tactile capabilities produced with a circular process", In *2023 IEEE International Conference on Soft Robotics (RoboSoft)*. **2023** 1–6, ISSN: 2769-4534.

[44] N. Willemstein, M. E. Imanian, H. van der Kooij, A. Sadeghi, "Pellet-based 3D printing of soft thermoplastic elastomeric membranes for soft robotic applications", *Materials & Design* **2025**, *258* 114589.

[45] L. Morita, A. Asad, X. Sun, M. Ali, D. Sameoto, "Integration of a needle valve mechanism with cura slicing software for improved retraction in pellet-based material extrusion", *Additive Manufacturing* **2024**, *82* 104045.

[46] R. Pang, M. K. Lai, H. H. Teo, T. C. Yap, "Influence of temperature on interlayer adhesion and structural integrity in material extrusion: A comprehensive review", *Journal of Manufacturing and Materials Processing* **2025**, *9*, 6 196.

[47] M. Bertolino, D. Battegazzore, R. Arrigo, A. Frache, "Designing 3D printable polypropylene: Material and process optimisation through rheology", *Additive Manufacturing* **2021**, *40* 101944.

[48] D. A. Rau, M. J. Bortner, C. B. Williams, "A rheology roadmap for evaluating the printability of material extrusion inks", *Additive Manufacturing* **2023**, *75* 103745.

[49] M. Elbadawi, J. Rivera-Armenta, B. Cruz, "Polymeric additive manufacturing: the necessity and utility of rheology", *Polymer Rheology* **2018**, *10* 43.

[50] W. P. Cox, E. H. Merz, "Correlation of dynamic and steady flow viscosities", *Journal of Polymer Science* **1958**, *28*, 118 619–622.

Table of Contents

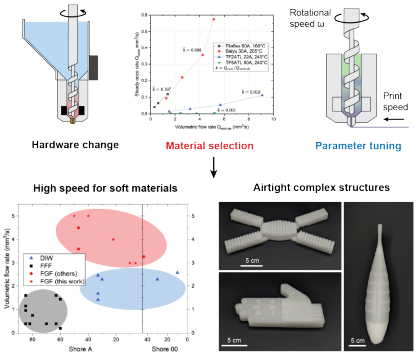

Fused Granulate Fabrication (FGF) is established here as a reliable and reproducible method for fabricating soft, airtight devices. Through coordinated optimization of hardware, material selection, and process parameters, this approach enables high-speed printing of thermoplastic elastomers with silicone-like softness and modulus. Systematic studies of extrusion stability, oozing behavior, and mechanical performance define a quantitative workflow that supports scalable, high-throughput manufacturing of soft devices.